Chemical Modification Mechanisms in Hybrid Hafnium Oxo-Methacrylate Nanocluster Photoresists for Extreme Ultraviolet Patterning

E.C. Mattson,[1] Y. Cabrera,[1] S.M. Rupich,[1] Y.X. Wang, [1] K.A. Oyekan,[1] T.J. Mustard,[2] M.D. Halls,[2] H.A. Bechtel,[3] M.C. Martin,[3] and Y.J. Chabal[1]

[1]Materials Science and Engineering Dept., University of Texas at Dallas, Richardson, TX 75080
[2]Schrödinger Inc., San Diego, CA 92121
[3]Advanced Light Source, Lawrence Berkeley National Laboratory, Berkeley, CA

Abstract

The potential implementation of extreme ultraviolet (EUV) lithography into next generation device processing is bringing urgency to identify resist materials that optimize EUV lithographic performance. Inorganic/organic hybrid nanoparticles or clusters constitute a promising new class of materials, with high EUV sensitivity from the core and tunable chemistry through the coordinating ligands. Development of a thorough mechanistic understanding of the solubility switching reactions in these materials is an essential first step toward their implementation in patterning applications but remains challenging due to the complexity of their structures, limitations in EUV sources, and lack of rigorous *in situ* characterization. Here we report a mechanistic investigation of the solubility switching reactions in hybrid clusters comprised of a small HfOx core capped with a methacrylic acid ligand shell (HfMAA). We show that EUV-induced reactions can be studied by performing *in situ* IR spectroscopy of electron-irradiated films using a variable energy electron gun. Combining additional *ex situ* metrology, we track the chemical evolution of the material at each stage of a typical resist processing sequence. For instance, we find that a crosslinking reaction initiated by decarboxylation of the methacrylate ligands under electron irradiation constitutes the main solubility switching mechanism, although there are also chemical changes imparted by a typical the post application bake (PAB) step alone. Lastly, synchrotron-based IR microspectroscopy measurements of EUV-irradiated HfMAA films enable a comparison of reactions induced by EUV vs electron beam irradiation of the same resist material, yielding important insight into the use of electron beam irradiation as an experimental model for EUV exposure.

Introduction

As density scaling drives electronic device components toward smaller sizes, high resolution and precision patterning techniques are playing an increasingly vital role. Extreme ultraviolet (EUV) lithography is anticipated to achieve the dimensions required by the next generation nanoelectronic devices owing to the much smaller photon wavelength (13.5 nm).[1, 2] Implementation of EUV lithography to adapt to the comparatively high photon energy naturally requires the development of compatible photoresist materials with properties tailored to optimize the response to EUV irradiation.[3] The current state-of-the-art photoresist materials for optical lithography, chemically amplified resists (CARs), are composed of a polymer matrix, a photoacid generator (PAG), and an acid quencher, and in some cases an acid generation promoter.[3-6] CARs are sensitized for UV wavelengths through an amplification mechanism that is initiated when PAGs become activated by UV photon absorption, leading to the generation of acids that disrupt the polymer network. While CARs have many appealing characteristics including a well-developed processing infrastructure, they also possess several drawbacks that limit the achievable patterning resolution. For example, CARs are susceptible to pattern collapse as features

become smaller, and appreciable acid diffusion[7] can hinder obtainable resolution. In addition, inhomogeneous distributions of the CAR components can further deteriorate resolution and lead to improper development of patterned features.[4, 8]

To circumvent the challenges posed by conventional resist materials, efforts have recently begun focusing on a new class of materials, hybrid inorganic-organic clusters, composed of an inorganic metal or metal oxide core or nanoparticle capped with organic ligands.[9-15] These systems, first developed at Cornell University,[9] possess properties that are inherently amenable to EUV patterning, such as comparatively strong EUV absorption from its inorganic core,[16] high etch resistance,[12] and the ability to tailor their chemistry through tunable ligand terminations. One such system that has demonstrated high sensitivity for negative-tone patterning consists of a hafnium oxide core capped with methacrylic acid (MAA) ligands (HfMAA). Along with their Zr-based analog (ZrMAA), HfMAA resists have demonstrated high-resolution patterning with EUV doses as low as 4.2 mJ/cm^2.[17-20] These results have generated an intense interest in the underlying EUV-resist interaction and solubility-switching mechanism of HfMAA and related systems. The first studies of the patterning mechanism in these materials[19-21] reached a number of important conclusions; first, the particle size following UV exposure increases from 3-4 nm to sizes approaching 1 μm,[19] indicating coalescence of the nanoparticles. A similar aggregation effect was observed in resist films subjected to a soft-baking step.[22] Second, the interpretation of *ex situ* IR spectra ruled out a photochemical crosslinking mechanism.[21, 23] Third, CO_2 was detected in unpublished work as a byproduct of the reaction in outgassing experiments,[24] and the dissociation of ligands was further supported by analysis of *ex situ* IR and core-level photoemission spectra of resist films subjected to comparatively high EUV doses (50-100 mJ/cm^2).[23] Taken together, a model emerged whereby solubility switching was attributed mostly to ligand exchange resulting from decomposition of the native ligands in alcohol developers. While consistent with initial data from various *ex situ* metrology, these studies could not derive an atomic scale description of this mechanism for lack of *in situ* characterization. Furthermore, Castellanos and coworkers reported IR, XPS and grazing incidence x-ray scattering measurements on Hf- Zr- and Ti-methacrylate clusters and proposed an alternate mechanism where solubility switching was characterized by a mechanism initiated by decarboxylation and subsequent crosslinking of the clusters.[25] Consequently, comprehensive *in situ* spectroscopic measurements would be useful to gain insight into the underlying mechanisms of these resists and enable operando quantification, particularly in the low-to-intermediate dose regime. Such measurements could address important observations of previous studies, such as the evolution of CO_2 and the apparent lack of consumption of unsaturated hydrocarbon following irradiation, and ultimately contribute to the optimization of HfMAA and related systems industrial-scale implementation. Such detailed studies are needed to provide insight into the underlying mechanisms of HfMAA and related systems.

Part of the difficulty in unraveling inorganic resist mechanisms lies in the complexity of the EUV-resist interaction. Absorption of EUV photons can result in the generation of photoelectrons from valence and shallow core levels. Chemistry resulting from EUV photon absorption can be induced through one of several pathways; for example, photoemission can lead to the creation of unstable radical cations that can decompose into smaller fragments and induce reactions. In addition, energetic electrons can also result in the emission of lower energy secondary electrons through inelastic scattering processes, which can in turn foster crosslinking reactions that affect solubility. An additional challenge in studying these interactions is the lack of EUV light sources; the only options for generation of 92 eV

photons are synchrotron radiation or large plasma sources that can be challenging to interface with *in situ* metrology. One approach to study the processes that take place following EUV photon absorption is to irradiate the thin resist film with a beam of energetic electrons[15, 26-29] to probe the effects of both primary photoelectrons and secondary electrons. For example, an incident beam of 90 eV electrons can serve both to probe the effect of energetic primary photoelectrons generated following EUV photon absorption, as well as to eject electrons from shallow core levels through impact ionization, just as in the case of EUV photons.

In the present work, we have demonstrated that this approach can be combined with *in situ* probes to track the evolution of resist chemistry under well-controlled conditions to mimic the reactions taking place during EUV irradiation. Specifically, we focus on understanding electron-induced solubility switching mechanisms of HfMAA resists, following each step of a typical industrial processing sequence: a post-application baking (PAB) step used following deposition to remove excess solvent, electron irradiation (in lieu of EUV irradiation), a post exposure baking (PEB) step, and finally development in isopropanol (IPA). The evolution of HfMAA at each stage is studied by *in situ* infrared (IR) absorption measurements as a function of electron-beam irradiation or thermal annealing, coupled with *ex situ* IR and x-ray photoemission measurements. The chemical specificity provided by IR spectra, supplemented by *ab initio* calculations, enables direct quantitative evaluation of the reactions that result from the electron-resist interaction. From these studies, we first find that the typical PAB step used to remove excess solvent results in condensation reactions involving extrinsic hydroxyl groups incorporated into the clusters, which in turn affects solubility. Next, analysis of IR spectra collected upon electron-beam irradiation show that, besides further condensation reactions induced by electrons, an additional mechanism involving crosslinking of neighboring clusters dominates the solubility switching. Additionally, we have evaluated the use of electron-beam irradiation as a model for EUV exposure to probe materials irradiated with EUV synchrotron radiation with IR microspectroscopy. Detailed crosslinking pathways leading to solubility switching mechanism are uncovered from spectral quantification and comparison to first principles models, providing a starting point for material optimization and a novel approach to the evaluation of inorganic resist mechanisms.

Methods

HfMAA and HfIBA Preparation

HfMAA and Hf-isobutyric acid (HfIBA), and Hf-benzoic acid (HfBA) clusters were prepared by a method reported previously,[12, 17] involving an 18-21 h reaction between hafnium isopropoxide and methacrylic acid (MAA), isobutyric acid (IBA) or benzoic acid (BA). In a typical synthesis, 1.20 g of hafnium isopropoxide was dispersed in 6.0 mL MAA and stirred at 75 °C for 15 min. Then 1.2 mL mixture of MAA and DI water (volume ratio of 9/1) was injected into the solution. The reaction mixture was stirred at 75 °C for 20 h. The reaction was stopped by adding DI water to the mixture to precipitate the product. The precipitation was washed twice by adding acetone and DI water followed by centrifugation at 8000 RPM for 5 min. The final powder was obtained after dried under vacuum at room temperature overnight. Particles prepared following this method were evaluated as being within the 2-3 nm range by dynamic light scattering (DLS) measurements (SI). This value is comparable to those reported for hafnium oxide nanoparticle-based photoresists.[22] Solutions of HfMAA or HfIBA were prepared by dissolution of the solid precursor material into propylene glycol monomethyl ether acetate (PGMEA) at nominally 3.0 or 0.75 wt%. In the case of HfMAA films, a 5 wt% excess of pure MAA was added to the solution to prevent

agglomeration of the clusters and displace incorporated water molecules (see SI). The solutions were sonicated for 5 min and passed through a PTFE syringe filter with 0.2 μm pores. Double-side polished silicon wafers were used as substrates for deposition of HfMAA or HfIBA; prior to coating, the wafers were first cleaned by sequential sonication in dichloromethane, acetone and methanol for 10 min intervals. Next, the wafers were cleaned in "Piranha" solution (3:1 sulfuric acid : hydrogen peroxide) for 20 min at 80 °C, before finally being rinsed thoroughly in deionized water. Thin films were prepared by spin-coating 125 μL of the HfMAA or HfIBA solutions onto the pre-cleaned Si substrates at 1500 RPM for 60 s inside of a nitrogen-purged glovebox to produce a thin film of the resist material (Fig. 1A). A PAB was performed under varying conditions as described in the main text.

In situ Infrared Spectroscopy and Electron Beam Irradiation

In situ IR spectroscopy was performed using a novel experimental setup incorporating a variable energy electron gun (Kimbell Physics, EGA-1012) mounted onto an ultrahigh vacuum (UHV) chamber equipped with differentially pumped KBr windows for IR transmission measurements (schematic in Fig. 1B). The electron gun was mounted such that the electron beam incidence was perpendicular to the direction of the IR beam propagation. The IR measurements were performed at Brewster's incidence (74° with respect to the sample normal), so that the electron beam was incident at 16° off normal to avoid moving the sample in between measurements. The sample temperature was monitored using a chromel-alumel (K-type) thermocouple spot-welded onto a Ta clip fastened to the substrate, and controlled either via resistive heating of the silicon substrate or through liquid nitrogen cooling of the sample holder. The base pressure at the time of the experiments was $\approx 1\times10^{-9}$ torr. IR spectra were collected using a Thermo-Nicolet Nexus 670 FTIR spectrometer and a mercury cadmium telluride (MCT)-B detector using 4 cm^{-1} spectral resolution and typically 2500 co-added scans.

Ex situ characterization

Ex situ IR spectroscopy was performed using a Thermo-Nicolet 6700 spectrometer equipped with a deuterated triglycine sulfate (DTGS) detector, located inside of a circulating N_2-glovebox.

X-ray photoemission spectroscopy (XPS) measurements were carried out using a Physical Electronics Quantum 2000 ESCA Microprobe equipped with a hemispherical mirror analyzer, employing $Al_{K\alpha}$ radiation. The measurements were performed at with a takeoff angle of 45° and a pass energy of 11.75 eV.

Spectroscopic ellipsometry was performed using a Horiba-Jovin UVISEL ellipsometer with the software program DeltaPsi2. In order to determine the thickness of the HfMAA or HfIBA layers, measurements on the Si substrates were first performed to determine the thickness of the native silicon oxide. Subsequent fitting of spectra for HfMAA or HfIBA films was performed using a Cauchy model for the dielectric function of the nanocluster films. Two different concentrations were used for the experiments reported in this study; measurements on 3.0 wt% films resulted in films within the 38-42 nm range, depending on the region of the coupon studied, while 0.75 wt% films were determined to be 8-10 nm in thickness.

Density Functional Theory Cluster Calculations

The results presented here were obtained using the Schrödinger Material Science Suite (Version 17-4). [30]. All DFT calculations used the Jaguar electronic structure program (Version 9.8).[31, 32] All structure derivatives and clusters were computed with DFT using the B3LYP hybrid functional and basis set LACVP**.[33-35] All energies reported are Gibb's Free Energies in kcal/mol, therefore including enthalpic and entropic contributions.

Synchrotron-based EUV Irradiation and IR Microspectroscopy

Synchrotron-based EUV irradiation of HfMAA films and subsequent examination using IR microspectroscopy were performed at the Advanced Light Source at Lawrence Berkeley National Laboratory (Berkeley, CA, USA). EUV irradiation was achieved using the Berkeley Microfield Exposure Tool (BMET) on 3.0 wt% HfMAA films prepared as described above without any PAB step. Distinct regions of the sample were exposed to doses ranging from 0-40 mJ/cm^2 and the films were subsequently developed in IPA so that the exposed regions could be readily identified in an IR microscope. IR microspectroscopy was performed at beamline 1.4 using a Nicolet Nic-Plan IR microscope with a 32× objective of numerical aperture of 0.65, equipped with a liquid nitrogen-cooled MCT-A detector. Spectra were generated from a total of 8000 co-added scans collected at 8 cm^{-1} spectral resolution and referenced to measurements performed on regions of the substrate in which no film was present.

Results

Vibrational characterization of HfMAA and HfIBA Films

Fig. 2A shows the IR absorption spectrum of a 3.0 wt% HfMAA film that was subjected to a 60 s PAB step using a hotplate programmed to 105°C in a N_2-purged glovebox, referenced to the spectrum of the substrate prior to HfMAA deposition. This absorption spectrum shows features that can be readily assigned to the modes of the carboxylate ligands; in the C-H stretching region, the asymmetric and symmetric stretches of the vinylic methylene groups give rise to bands at 3100 and 3019 cm^{-1}, respectively. Absorption arising from the split CH_3 asymmetric stretches of the methyl groups can be observed at 2990, 2975, and 2950 cm^{-1}, and from the CH_3 symmetric stretch at 2923 cm^{-1}. A band at 2855 cm^{-1}, characteristic of the CH_2 symmetric stretch of a methylene group bonded in an alkyl configuration, is not intrinsic to pure HfMAA but rather indicative of an impurity. The band at 1650 cm^{-1} is assigned to the C=C stretch of the vinylic methylene groups, and the intense mode centered at 1579 cm^{-1} to the carboxylate O-C=O asymmetric stretching. The intense bands in the 1340-1500 cm^{-1} region are due to the asymmetric and symmetric CH_x deformation modes that are strongly coupled to the symmetric O-C=O stretching modes, while the band at 1250 cm^{-1} is assigned to the rocking vibrations of the vinylic methylene groups. The remaining modes in the 800-1150 cm^{-1} region are assigned to various librational modes of the methyl and methylene groups, and the bands in the 600-750 cm^{-1} region arise from a combination of Hf-O stretching and O-C=O angle bending.

Unexpectedly, the spectrum also shows pronounced bands in the OH stretching region (broad and sharp bands at 3420 and 3660 cm^{-1} due to hydrogen bonded and isolated hydroxyl groups, respectively). Since ideal HfMAA cluster do not have any hydroxyl groups, their presence indicates that the system is prone to pick up water leading to OH functionality, which could contribute to further chemical reactions. These

OH contributions are also detected in the measurements of the solid state precursor prior to dissolution, indicating that water incorporation occurs even before spin casting.

Consideration of analogously prepared HfO_x carboxylate clusters but with IBA as the capping ligand is particularly interesting because it provides a useful comparison to distinguish the role played by vinylic hydrocarbon. A schematic drawing of the composite HfIBA is shown in Fig. 1B. Unlike HfMAA, HfIBA lacks vinylic methylene groups, instead having an additional methyl group. This difference is reflected in the IR spectrum of analogously prepared 3.0 wt% HfIBA films, as shown in Fig. 2B. Here, no features associated with vinylic hydrocarbon (3100, 1650 cm^{-1} modes in Fig. 2A) are observed; instead, there is an increase in the intensity of the modes associated with the methyl groups (2970, 2933, 2876 cm^{-1}), as well as slight shifts in the carboxylate stretching and CH deformation modes (1400-1600 cm^{-1}), and different modes associated with CH_3 librations (800-1300 cm^{-1} region). HfIBA clusters are therefore used as a control system to understand the role of the vinylic groups in the chemistry of HfMAA.

Effect of PAB

A PAB, usually performed under N_2 or air ambient at relatively low temperature (80-120°C), is commonly used during photoresist processing to remove residual solvent. We investigated the effect of PAB on HfMAA clusters to monitor solvent removal and assess which chemistry takes place if any, and whether the solubility of the material is impacted. We performed PABs on HfMAA films under different environments (N_2, air, and UHV) and with different heating methods (either a hotplate or resistive heating of Si substrate) to further understand the role of PAB conditions. For that study, we tested the solubility of HfMAA films in isopropanol, in which the material should be completely soluble. We found (results summarized in Fig. S2) that PAB reduces the solubility of the films, and that the extent of the solubility switching is determined by the conditions used for the PAB. Air and UHV/resistive heating PABs were most effective in switching solubility, resulting in solubility switching of ≈5.5-6.5% of the starting film.

To understand the thermally-induced chemistry underlying the decreased solubility, we performed *in situ* IR absorption measurements of 0.75 wt% films subjected to a UHV annealing step. The anneal was performed by resistively heating the Si substrate to a temperature of 105°C maintained for 60 s. We note that the resistive heating PAB delivers a greater thermal load than the hotplate/N_2 ambient PAB for several reasons; first, the substrate itself is directly heated, rather than relying on conduction of heat from an external body. Second, the sample side of the substrate is not exposed to a high pressure of gas molecules that effectively dissipate the heat transferred to the substrate. In an N_2 ambient, the film itself never reaches the same temperature as on the hotplate; in contrast, heat transfer to the ambient environment is negligible under UHV, leading to a higher sample temperature. Lastly, the time required to reach the target temperature and cool back down is longer in the case of the resistive heating PAB; while the sample is held at the target temperature (105°C) for one minute, approximately 1 minute is required to reach temperature and 2 minutes are required to cool back to 40°C. With these combined effects, the overall thermal load received by the sample is larger in the case of the UHV PAB, which should be kept in mind in the sections that follow.

The resulting differential spectrum following the UHV PAB (*i.e.,* the IR spectrum following annealing referenced to the spectrum collected immediately before annealing) is shown in Fig. 3A. A number of spectral changes are clear upon inspection, and we discuss them in turn. First, there is a marked loss of both isolated and hydrogen-bonded hydroxyl (sharp and broad modes at 3660 and 3420 cm^{-1},

respectively). Second, losses are observed at many of the frequencies of the MAA ligands, particularly the C-H stretching region (2800-3100 cm^{-1}), the carboxylate asymmetric stretching band 1580 cm^{-1}) and the O-C=O symmetric stretching/CH_x deformation region (1400-1500 cm^{-1}). In addition, new modes at 1529, 606, and 508 cm^{-1} are observed as positive bands and can be considered markers of a thermally-induced reaction pathway. We address the origin of these changes in the discussion section.

Spectral Evolution following Electron Beam Irradiation

Having identified spectral markers associated with thermally-induced chemistry, we can now consider the response of HfMAA films following bombardment of energetic electrons. We use 90 eV electrons for the initial studies, as this energy is close to both the energy of the photoelectrons produced following ionization from valence levels and the energy of the EUV photon beam (see the SI section for details on irradiation with electrons of various energies). We first consider the case in which a 0.75 wt% film was prepared with a typical hotplate PAB, performed under N_2 ambient for 60 s at 105°C prior to loading into the UHV chamber. Thinner (0.75 wt%) films were used for all electron beam irradiation studies to minimize sample charging effects. Fig.3B shows the differential spectrum of the film following irradiation with 90 eV electrons with a total dose of 40 $\mu C/cm^2$. Comparing to the differential spectrum representative of thermally induced changes (Fig. 3A), several similarities and differences are apparent. First, intense losses are observed at all frequencies in which the ligand modes absorb, indicating an overall loss of ligand or breaking of bonds to form another chemical species. In addition, weak positive bands are present at 1521 and 608 cm^{-1}, which were previously associated with thermally induced reactions. In contrast to the spectrum in Fig. 3A, the spectrum in Fig. 3B shows a significant positive feature in the 2800-3000 cm^{-1} region, in which the C-H stretches of alkyl CH_2 and CH_3 functional groups absorb. The strengthening of these features indicates that 90 eV irradiation can also convert MAA ligands into alkyl moieties. Importantly, this treatment leads to solubility switching of the film, (Fig. S3) tested using isopropanol as the developer. Since the weak positive band at 1521 cm^{-1} is partially obscured in the *in situ* spectra by the intense negative feature at 1580 cm^{-1}, spectra collected *ex situ* (Fig. S4) were recorded and also show the formation of a slightly blueshifted component (≈1600-1610 cm^{-1}), corresponding to 20-30 cm^{-1} shift of the O-C=O asymmetric stretching peak and confirming the interpretation of the *in situ* measurements.

Spectral changes associated with electron-specific chemistry can be distinguished from thermal chemistry induced by the electron beam by saturating the thermal reactivity prior to electron beam irradiation. We accomplished this by first performing a PAB step with resistive heating inside of the UHV chamber prior to irradiation for 3 minutes at 105°C, which we found was sufficient to fully saturate thermally induced changes observed in IR spectra. Fig. 3C shows the differential spectrum of a HfMAA film subjected to the aforementioned UHV PAB and subsequently irradiated with 90 eV electrons for a total dose of 40 $\mu C/cm^2$. The spectrum is referenced to that collected immediately following the annealing step, highlighting only changes due to electron irradiation. Comparing to the spectra in Figs. 3A-B, it is clear that the spectral features associated with the thermal chemistry of the system, in particular the positive feature observed at 1528 and 1521 cm^{-1} in Figs. 3A-B, respectively, is notably absent in the spectrum in Fig. 3C. The spectrum in Fig. 3C does, however, show the distinct positive alkyl CH peaks between 2800-3000 cm^{-1}, as well as losses at the frequencies of all of the ligand modes as was observed in Fig. 3B. In addition, since considerably less hydroxyl is present in the film following the UHV PAB as compared with the hotplate PAB, the formation of an O-H stretching feature following irradiation can be more clearly observed in the spectrum in Fig. 3C (3720 cm^{-1}). In contrast, intense

losses at the frequencies of the O-H stretches obscure the positive OH feature in the spectrum in Fig. 3B. These data demonstrate unambiguously that thermal reactions are also initiated by the incident electron beam in addition to electron-specific reactions.

Additional insight into the changes induced by electron beam irradiation can be obtained through *ex situ* XPS measurements. Such measurements provide complementary quantitative analysis of the elemental composition and the chemical states of the elements present in the films as-prepared (with hotplate PAB, 105°C for 60s) and after irradiation. Figure 4 shows the C1s, O1s, and Hf4d levels of 3 wt% HfMAA as-prepared and after 90 eV irradiation. The spectra of the irradiated material show several notable differences relative to the as-prepared material: First, the overall intensities of the H4d and C1s spectra appear elevated in the irradiated spectra relative to the as-prepared spectra, while the overall intensity of the O1s shows minimal change. Second, the C1s spectrum shows elevated intensity in the peak centered at 288.5 eV due to unoxidized C relative to the component at 292.3 eV assigned to carboxylate functional groups. The elemental composition (at. %) of the films derived from these spectra is shown in Table 1. The data show that the 90 eV electron irradiation has the effect of lowering the relative oxygen content of the film, while correspondingly elevating the relative C and Hf content.

Analogous UHV annealing and electron beam irradiation of HfIBA provide an important control to probe the role of the vinylic methylene groups in thermal and electron-driven reaction pathways. Fig. 5A shows the differential spectrum of a 3 wt% HfIBA film subjected to a 60s UHV anneal at 105°C under conditions analogous to those that produced the spectrum in Fig. 3A. Upon comparison of the differential spectra from 90 eV irradiation of HfMAA and HfIBA (Figs. 3A and 4A, respectively), a number of similarities are observed. Both spectra show a loss of all ligand modes present in the spectrum of the as-prepared material, including the extrinsic hydroxyl groups, and no evidence of alkyl hydrocarbon formation is observed. For HfMAA, a positive feature is observed at 1531 cm^{-1}, as compared to 1521 cm^{-1}. It is interesting to note that the carboxylate O-C=O asymmetric stretching mode in the case of as-prepared HfIBA (Fig. 2B) is centered at 1586 cm^{-1}, i.e. 7 cm^{-1} higher in frequency than the corresponding mode in HfMAA. Similarly, the positive feature formed by annealing HfIBA (1531 cm^{-1}) is observed at a frequency ≈10 cm-1 higher than the corresponding mode formed by annealing HfMAA (1521 cm^{-1}). The similarity in these relative carboxylate peak positions points strongly to a carboxylic origin of the mode formed upon annealing HfMAA or HfIBA. In addition, both differential spectra in Figs. 3A and 4A show a positive feature at 600 cm^{-1}, within the spectral region expected for Hf-O stretching. Having identified notable similarities in the thermal chemistry between HfIBA and HfMAA, we next compare the effect of 90 eV electron-beam irradiation. Fig. 4B shows the differential spectrum obtained following irradiation of an HfIBA film with a dose of 41 $\mu C/cm^2$. Here, a PAB was performed prior to loading into UHV using a hotplate programmed to 105°C under N_2 ambient to enable direct comparison to the spectrum in Fig. 3B. As was observed for HfMAA, irradiation of HfIBA results in losses at all of the frequencies associated with the ligand in the as-prepared material, as well as the appearance of positive features at 1531 cm^{-1} and 600 cm^{-1}. In contrast to irradiated HfMAA, the spectrum of irradiated HfIBA does not show any evidence for the formation of alkyl hydrocarbon, confirming that the vinylic methylene groups in HfMAA are directly involved in the reactions that drive solubility switching.

<u>Reaction products from Low-temperature Irradiation</u>

The *in situ* IR spectra of HfMAA clearly show that irradiation with 90 eV electrons (as well as lower energy electrons, as discussed in Fig. S5) leads to formation of alkyl hydrocarbon. Another

important component needed to derive the reaction mechanism is the identification of intermediate structures and volatile reaction products. One way to retain the volatile reaction products, which otherwise rapidly desorb from the film at room temperature, is to cool the sample during irradiation, thereby inhibiting diffusion and desorption of the reaction products produced from the irradiation. This approach makes it possible to detect the volatile reaction products by IR spectroscopy and to "freeze" the activated reactions so that they can be studied in a stepwise fashion, as detailed below. Fig. 5 shows the result of such an experiment on a 0.75 wt% HfMAA film. After a hotplate PAB under N_2 ambient at 105°C for 60 s, a reference spectrum is recorded. For easy comparison, Fig. 5A shows the spectrum of the as-prepared material. Fig. 5B shows the differential spectrum of the film following 122 $\mu C/cm^2$ irradiation 90 eV electrons with the substrate at -173°C during both the irradiation and IR measurements. Several important features are observed: first, losses are again observed at all frequencies associated with the ligand modes of the as-prepared material. Second, a positive feature in the alkyl CH region is observed as a broad envelope overlapping with losses of the methyl and vinylic methylene modes. Similarly, a positive OH feature between 3600-3700 cm^{-1} is observed and overlapping with a sharper loss of the OH feature at 3650 cm^{-1} in the as-prepared material. Third, a very sharp, intense peak is present at 2337 cm^{-1} that was not previously observed in any of the spectra collected at room temperature. Based on the elements present in the material, the only functional group that could be expected to absorb at this frequency is CO_2, which has an intense O=C=O asymmetric stretch at 2349 cm^{-1}. The remaining low-frequency region of the differential spectrum shows changes that closely resemble those observed with room-temperature irradiation. While the spectrum in Fig. 5B clearly shows that CO_2 is a dominant byproduct of the irradiation, the spectrum is a superposition of the losses of the ligand modes with the absorption spectra of the trapped reaction products.

The spectra of the reaction products can be distinguished from the strong losses of the ligand modes by heating up the sample to drive out the volatile reaction products and use the initially irradiated sample as a reference spectrum (i.e., Fig. 5B). Fig. 5C shows the resulting spectrum of the irradiated sample after annealing to 20°C for 1 min before cooling back to -173°C. The spectrum is referenced to the spectrum collected after irradiation so that only the changes due to the 20°C annealing step are present in the differential spectrum. Negative bands are now associated with functional groups that are eliminated (desorbed) or consumed by the annealing process, and positive bands with bond or functional group formation. Beginning at the high wavenumber region of the spectrum, a loss of hydroxyl groups is evidenced by a negative peak at 3625 cm^{-1}. In the CH region, we observe a series of positive peaks at exactly the frequencies of the methyl asymmetric and symmetric stretching modes in as-prepared HfMAA. At the same time, negative bands are observed at 2915 and 2844 cm^{-1}, frequencies that are typical of alkyl CH_2 asymmetric and symmetric stretching vibrations, respectively. The sharp band at 2337 cm^{-1} assigned to trapped CO_2 now appears as a negative feature, indicating that the CO_2 has either desorbed from the film or reacted with another species. In the carboxylate region, positive features are observed at 1579 and 1525 cm^{-1}, which correspond to the frequencies of the carboxylate O-C=O asymmetric stretch in the as-prepared material and after a PAB treatment, respectively. The observation of positive bands at the frequencies of the corresponding carboxylate and methyl peaks in HfMAA indicates that a fraction of the fragments produced from irradiation actually *recombines* following annealing to form more stable carboxylate functional groups. We can estimate the relative amounts of carboxylate lost and reformed from irradiation and subsequent annealing to 20°C, respectively, by computing the integrated area of the carboxylate peaks (1500-1600 cm^{-1}) in the spectra

in Figs. 5B-C. In doing so, we find that the positive carboxylate peaks in Fig. 5C correspond to ≈20% of the intensity of the carboxylate peaks lost in Fig. 5B, and can thus be interpreted as 20% of the CO_2 molecules generated from irradiation reacting with other products to decay back into a carboxylate ligand. This finding has important implications for the EUV irradiation analog, where exposure is performed at room temperature and liberated fragments are therefore mobile.

The results derived from these low-temperature irradiation measurements offer unique insight into the dynamics and reaction products of the system. One unambiguous result is that CO_2 is generated as a result of the irradiation at the expense of the carboxylate ligands, consistent with findings from previous studies of analogous systems.[19, 22] Of these CO_2 molecules formed, some fraction (an estimated ≈20%) will recombine with other products/fragments to reform carboxylate groups. Somewhat less clear is the chemical identity of the products responsible for the OH and CH bands at 3625 and 2915/2844 cm^{-1}, respectively, that are removed following annealing to 293K. In the discussion section, we discuss the reaction mechanisms associated with both the thermal and electron-specific crosslinking pathway, with input from DFT cluster models. We thus propose several models to correlate the spectral changes observed following annealing and irradiation with the underlying chemistry of the system.

Comparison to Synchrotron EUV Irradiation of HfMAA (*ex situ* Spectroscopy)

Evaluation of electron-beam irradiation as an experimental model for understanding chemistry induced by EUV photons is an important question with implications for understanding EUV resist mechanisms general. In order to compare the effects of EUV and electron beam irradiation, we performed measurements on HfMAA films irradiated with EUV synchrotron radiation (13.5 nm). We were able to examine relatively small irradiated regions by performing IR microspectroscopy at beamline 1.4 at the Advanced Light Source (ALS). Following EUV exposure, the films were developed so that the irradiated regions could be clearly identified and the remaining uncovered regions used a reference. No PEB was applied. To produce spectra that mimic the differential spectra collected *in situ,* we processed the data by subtracting the spectra of non-irradiated HfMAA from the spectra of irradiated and developed HfMAA, so as to demonstrate the differences resulting from irradiation. The resulting differential spectra, corresponding to doses ranging from 2.5-40 mJ/cm^2, are shown in Fig. 7. Several clear trends are observed in the spectra with increasing EUV dose; first, the positive features corresponding to alkyl hydrocarbon (2800-3000 cm^{-1}) increase continuously with dose. Second, there is a clear blueshift in the frequency of the carboxylate asymmetric stretch of about 20 cm^{-1}, and the magnitude of the blueshifted component grows with increasing EUV dose. Interestingly, though, no band is observed at 1520 cm^{-1} as was the case for HfMAA films subjected to annealing and electron-beam irradiation.

Discussion

Structural Changes following PAB: Thermal Reaction Pathways

The results above show that the PAB modifies the chemistry of HfMAA more than would be expected for simply removing any residual solvent, and that the solubility of the films is reduced in absence of any irradiation. Such delocalized solubility switching is detrimental for patterning applications, where complete removal of the (positive tone) resist in unexposed areas is essential to subsequent processing and deposition steps. In addition, thermal reactions identified with PAB also

appear to be activated by electron beam irradiation, as evidenced by the differential spectra in Figs 3A-B. The thermal reaction pathway is therefore an important component to the overall solubility switching mechanism that needs to be understood.

We observe thermally induced spectroscopic changes (e.g., positive feature in the 1520-1530 cm^{-1} region and at 600 cm^{-1}) as shown in Figs. 5A-B, respectively. We can therefore conclude that the thermal mechanism is independent of the vinylic groups present in HfMAA. In addition, we observe similar shifts in the carboxylate peaks following annealing of analogous particles capped with benzoic acid ligands (Fig. S6), suggesting that the origin of these shifts is typical of carboxylate-capped nanoparticles and independent of the terminal groups. We now consider the structural origin of these changes and their relationship to solubility. One of the most prominent changes in the spectra following PAB is the loss of both the isolated and hydrogen-bonded O-H features, as well as the development of a positive band at 600 cm^{-1} in both the spectra of annealed HfMAA and HfIBA films (Figs. 3A and 5A, respectively). Since the OH stretching band at 3650 cm^{-1} in particular is associated with hydroxyl groups bonded to Hf, the loss of these modes suggests a change in the coordination of the Hf centers, which in turn leads to a shift of the O-C=O asymmetric stretch. We further can verify that incorporation and loss of hydroxyl groups is directly correlated to the shift of carboxylate frequency by performing controlled *in situ* water dosing and annealing experiments, as described in Fig. S7. These results demonstrate a direct link between the incorporation of hydroxyl groups and the frequency of the carboxylate asymmetric stretch.

Having established that the loss of hydroxyl groups plays a central role in the thermal pathway, we performed DFT modeling of representative small HfMAA clusters to correlate the spectral changes observed following PAB to underlying chemistry. To differentiate among several different structures that can result from (de)hydroxylation of a methacrylate-coordinated HfO_x cluster, two theoretical results need to be considered: first, the frequency of the O-C=O asymmetric stretching mode of chelated methacrylate ligands is considerably lower than that of bridging ligands. Second, hydroxylation of bridging O atoms results in a blueshift of the O-C=O asymmetric stretch frequency. With these considerations, the reaction that most closely reproduces our experimental results is depicted in the DFT-optimized structural models of Figs. 8A-B. The structure of the cluster was chosen so as to capture the essential characteristics of the HfMAA system, namely the mixed conformations of the methacrylate groups (bridging and chelating) as well as the presence of hydroxyl groups. The inherently amorphous nature of the material unfortunately makes it impossible to represent the system stoichiometrically within a single cluster; however, the model presented here takes into account all of the chemical moieties contributing to the thermal reactivity of the system with the goal of understanding their vibrational frequencies. Importantly, the surrounding matrix would be expected to have a minimal perturbation on the vibrational frequencies except in cases of hydrogen bonding, which primarily impacts hydroxyl groups and has been addressed above. With this approach we treat the system as a 2 Hf-atom cluster with 6 methacrylate ligands and one bridging O atom (Fig. 8A). Since each Hf atom is coordinated to 3 chelated methacrylate ligands of charge of -1 and one bridging O atom, the oxidation state of each Hf atom is 4+. We note that the as-prepared clusters consist of a mixture of bridging and chelating ligands; for simplicity and ease of interpretation, we represent only chelated ligands in the non-hydroxylated state. The structure in Fig. 8B represents the evolution of the clusters following interaction with water vapor. Here, the water molecule has dissociated to hydroxylate the bridging O atom and form one bidentate and one monodentate hydroxyl group. In order to balance the charge

state and coordination of the two Hf centers (+4 for each Hf atom), one of the chelated ligands is transformed to a bridging ligand. The incorporation of a water molecule in the complex in Fig. 8A forms the complex in Fig. 8B is slightly exothermic, with a gain in the Gibb's free energy of 7 kCal/mol. The calculated vibrational frequency of the O-C=O asymmetric stretch of the chelated methacrylate ligands in the non-hydroxylated structure (Fig. 8A) is 1560 cm^{-1}, whereas that of the bridging ligands in the hydroxylated structure (Fig. 8B) is 1598 cm^{-1}. This ≈40 cm^{-1} shift is similar to the 55 cm^{-1} shift of the carboxylate peak we observe experimentally upon annealing. We also note that the extent of the blueshift of the carboxylate peak is dependent on the types of ligands coordinated to the H atom.

In a similar model, we find that exchanging two of the chelated methacrylates in Fig. 8B with hydroxyl groups increases the O-C=O asymmetric stretch of the bridging methacrylate to 1626 cm^{-1}, corresponding to a 66 cm^{-1} shift, indicating that the different chemical species bound the Hf atoms differently impact the extent of the shift (Fig. S8). The calculated shift of 40 cm^{-1} for the water-induced chelating-bridging transition is therefore in reasonable agreement with the 55 cm^{-1} shift observed following the PAB and consistently accounts for the frequency shifts observed in our experimental spectra. Therefore, the essential feature of the reactions following PAB (i.e. rise to the band at 1520 cm^{-1}) is captured qualitatively by a model in which the structure in Fig. 8B is converted to that in Fig. 8A.

The reaction in Figs. 8A-B explains many of the features observed in water dosing and annealing cycles, and is consistent with a metastable, reversible HfMAA/water interaction. Such a process does not, however, account for the decrease in solubility in the case of the samples subjected to PAB under N_2 or UHV or the Hf-O stretching mode that appears at 605 cm^{-1} with annealing. We propose that the origin of solubility switching is a condensation reaction that occurs when the hydroxyl groups are liberated from the Hf centers to form a water molecule and a bridging O that links adjacent clusters through formation Hf-O-Hf bonds. In fact, the observation of a band at 605 cm^{-1} (Fig. 3A) following annealing confirms the formation of Hf-O-Hf linkages. This mechanism also accounts for the observation that the PAB performed under air ambient results in the greatest extent of solubility switching of the conditions investigated (Fig. S2).

To summarize, the thermal reactivity of HfMAA is primarily characterized by reactions involving native hydroxyl groups. These hydroxyl groups, the majority of which are likely formed from reaction with water during preparation of the particles, induce chelating-bridging transitions of the methacrylate groups. Upon annealing, the hydroxyl groups undergo condensation reactions to produce Hf-O-Hf bonds and water, which in turn reduces the solubility in localized regions of the films, (e.g., as in Fig. S9). Following these reactions, nearby bridged methacrylate ligands chelate to balance the oxidation state, resulting in a considerably redshifted carboxylate frequency, as depicted in Fig. 8.

Cross-linking Reaction Pathway

The data in Figs. 3, 4 and 6 provide mechanistic insight into the reactions that lead to the solubility switching following electron or EUV irradiation. While we have shown that a condensation reaction initiated either thermally or by energetic electrons can reduce the solubility of the films, the data in Figs. 3B-C demonstrate the presence of another mechanism specific to the interaction between ligands containing a vinylic methylene group and energetic electrons. Our experimental data have indicated that this electron-specific pathway is characterized by the loss of vinylic groups and formation of alkyl hydrocarbon groups. In addition, the data in Fig. 6 demonstrate unambiguously that CO_2 is a

product of this reaction, pointing to a decarboxylation pathway as previously proposed by Castellanos et. al. for this system[19, 25] and experimentally observed in other metal-carboxylate resist materials.[36, 37]

Based on the discussion below, we argue that this pathway can be described by the scheme in Fig. 9. Consider first the structure of a methacrylate ligand within an HfMAA cluster; we represent these ligands as chelated structures in Fig. 9. The Hf atoms can additionally be coordinated to either bridging oxygen atoms linking to another Hf, hydroxyl groups, or additional methacrylate ligands. Following absorption of an EUV photon by a Hf atom, excitation from shallow core levels will lead to generation of an energetic photoelectron, leaving behind an unstable radical cation. In the electron beam irradiation analog, the initiation results from impact ionization, where an electron scatters inelastically from a metal center to eject an electron, leaving behind a radical cation. Since the data in Fig. 6 identify CO_2 as a byproduct, we can infer cleavage of both the Hf-O and C-C bonds in the initial molecule and decomposition of the ligands as depicted in Fig. 9A. The asymmetric stretching frequency of the trapped CO_2 molecules (2337 cm^{-1}) is very close to its value observed in the gas phase (2349 cm^{-1}), ruling out the possibility that the trapped CO_2 molecules are in a charged or radical state and further supporting the decomposition scheme in Fig. 9A. While CO_2 leaves the film as an inert byproduct of the reaction, the remaining Hf cation and propenyl radical remain, and both can potentially contribute to subsequent reactions. The concomitant loss of features associated with vinylic CH_2 (CH_2 asymmetric stretch at 3100 cm^{-1} and C=C stretch at 1650 cm^{-1}) and formation of alkyl hydrocarbon (positive feature between 2800-3000 cm^{-1} in Figs. 3B-C) indicate vinylic to alkyl conversion. This observation is consistent with both the linking of a propenyl radical to a neighboring methacrylate group as in Fig. 9B, or potentially through the direct reaction of two vinylic methylene groups. The latter pathway can be ruled out as the dominant mechanism, however, since direct crosslinking through two neighboring vinylic methylene groups would not result in decarboxylation/CO_2 formation, as observed in our data. The structure resulting from the propene attachment to a neighboring methacrylate ligand (Fig. 9B) is also a radical. This structure can react with the vinylic group on another neighboring methacrylate ligand to form a crosslinked radical structure that links adjacent clusters, as in Fig. 9C. In addition to crosslinking initiated by the propenyl radical, the Hf^+ cation left behind following decomposition of the methacrylate ligand can also serve to initiate further reactions that induce solubility switching. For example, the Hf^+ cation can react directly with the vinylic (or hydroxyl) group of a neighboring methacrylate to produce a larger cation structure as shown in Fig. 9D. If this neighboring methacrylate is in an adjacent cluster, this reaction will contribute to solubility switching. The resulting cation formed can also continue to react, inducing additional crosslinks that participate in the overall solubility switching. In yet another pathway, a Hf(IV) cation can accept an electron to yield Hf(III). The resulting Hf(III) complex would also be expected to be very reactive, and could also bind directly to the methacrylate group of a neighboring electron to form a Hf-C crosslink, which could in turn continue to propagate crosslinking.

We note that the observation of alkyl formation taken on its own is not necessarily evidence that the clusters are crosslinked; *i.e.,* it is conceivable the reaction in which the structure in Fig. 9A is converted to that in Fig. 9B could in principle produce an alkyl hydrocarbon signature without actually forming the structure in Fig. 9C, in which a crosslink is formed between adjacent clusters. We rule out however these two pathways based on several observations. First, the formation of the structure in Fig. 9B on its own would not be expected to give rise to any solubility switching, since no links are formed between adjacent clusters. More quantitatively, however, the progression from Fig. 9B to Fig. 9C can be inferred from the experimental differential spectra. Note that the reaction between 9A-9B results in the

net loss of one carboxylate group and one vinylic group, while one carboxylate and two vinylic groups are lost through the net process going from Fig. 9A-C. Similarly, if the radical structure in Fig. 9C continues to propagate and form additional crosslinks, additional vinylic groups will be consumed while carboxylates are not.

These scenarios can be tested against our experimental data by comparing the relative consumption of vinylic and carboxylate groups in the differential spectra following electron beam irradiation. Specifically, we evaluate the area ratio of vinylic and carboxylate-specific markers taken from the *ex situ* spectrum of the sample irradiated to produce the spectrum in Fig. 3C. In particular, we use the area ratio of the C=C stretch to O-C=O asymmetric stretch as a relative metric for the vinylic : carboxylate composition ratio. Next, we evaluate the same ratio from negative bands in the differential spectrum in Fig. 3C (*i.e.,* the spectrum following electron-beam irradiation). Dividing the area ratio generated from the differential spectrum in Fig. 3C by the corresponding area ratio of the as-prepared material following PAB therefore gives the *relative* consumption of vinylic to carboxylate groups. In performing this quantification, we find that the vinylic : carboxylate ratio in the spectrum in Fig. 3C is 2.75-3× greater (depending on the choice of baseline and integration window for carboxylate peak) than in the case of the as-prepared film subjected to a UHV PAB (Fig. S10). Thus, for every carboxylate group consumed, ≈2.5-3 vinylic groups are consumed. From these data, we can therefore infer that the reaction underlying the alkyl CH formation must involve crosslinking through radical propagation such as that depicted in Fig. 9C.

The last aspect of the mechanism in Fig. 9C that remains to be verified is that the alkyl hydrocarbon formed upon irradiation actually remains coordinated to carboxylate groups that bind to Hf atoms and is therefore responsible for the solubility switching. For example, it is conceivable that the alkyl hydrocarbon formed could result from the sequential linking of 2 or more propenyl radicals liberated following decomposition of the methacrylate ligands as in Fig. 9A without any actual coordination to the carboxylate groups bound to the Hf atoms. Below, we argue that changes in the carboxylate peak position following irradiation can be directly linked to crosslinking and provide a direct indication that the alkyl fragments formed provide crosslinks between adjacent carboxylate groups. Recall that following 90 eV irradiation, we also observed the formation of a positive component slightly blueshifted from the position of the carboxylate asymmetric stretching peak in as-prepared HfMAA (Fig. S4). Similarly, the difference spectra of EUV-irradiated HfMAA clearly showed a ≈20 cm^{-1} blueshifted carboxylate peak that increased concomitantly with EUV dose and alkyl hydrocarbon formed. By performing DFT calculations of the vibrational frequencies of HfMAA clusters with a single alkyl crosslink, we have found that the presence of the crosslink increases the vibrational frequency of the carboxylate groups by an amount that is in close agreement with that observed experimentally. Fig. 10 shows two representative structural models used for the calculations; Fig. 10A represents the local structure of a single chelated methacrylate ligand, analogous to the schematic diagram of the starting HfMAA structure shown in Fig. 9A. The calculated frequency of the asymmetric carboxylate stretch is 1555 cm^{-1}. The structure in Fig. 10B is analogous to the crosslinked schematic in Fig. 9C, and has two distinct modes characterized by O-C=O asymmetric stretching at 1549 and 1573 cm^{-1}. The displacements associated with the 1573 cm^{-1} mode are primarily due to the asymmetric bond stretching/compression of the carboxylate group labelled **1**, while those of the 1549 cm^{-1} mode involve both the asymmetric displacement of the carboxylate group labeled **2** as well as CH_3 and CH_2 deformation of the adjacent hydrocarbon groups. Importantly, these data demonstrate that a ≈20 cm^{-1}

blueshift of the carboxylate asymmetric stretch can be expected upon crosslinking, consistent with the spectra collected following both EUV and electron beam irradiation.

The above mechanism is supported by a large body of experimental work on smaller inorganic/organic clusters with analogous ligand coordination.[38-41] In these studies, clusters with well-defined sizes determined through x-ray crystallography were synthesized, comprised of either $Hf_4O_2(Mc)_{12}$ or $Zr_4O_2(Mc)_{12}$. It was shown that these clusters readily cross-link through radical polymerization in solution phase, giving rise to larger insoluble networks, very similar to those reported here. Therefore, although the crosslinking mechanism proposed here is fundamentally different than the mechanism proposed by Ober, Gianelles and coworkers, it is in agreement with previous observations of radical-induced polymerization in similar and well-defined systems.

EUV vs Electron Beam-induced Solubility Switching Mechanisms

The data in Figs. 3 and 7, allow for comparison of chemistry induced by EUV photons and 90 eV electrons and therefore enable an evaluation of electron-beam irradiation as a model for EUV-induced chemistry in general. We first note that the differential spectra obtained following EUV irradiation and development (Fig. 7) exhibit a continuous increase in both the alkyl hydrocarbon signature (2800-3000 cm^{-1}) and the blueshifted carboxylate (1600 cm^{-1}), features we identified as markers of crosslinked ligands. The main difference between the spectra resulting from EUV irradiation vs electron-beam irradiation is the overall absence of the positive band at 1520 cm^{-1} in the case of the EUV-irradiated spectra. This indicates that EUV irradiation does not induce thermal chemistry, in contrast to electron irradiation. For the latter, the short inelastic mean free path (IMFP) of low energy electrons ensures that the electrons dissipate the majority of their energy through various scattering mechanisms within the first few nm of the surface, confining the electron-resist interaction to a shallow surface region. The majority of the energy of the electron beam is then dissipated into a comparatively small volume of the film, resulting in the delivery of considerable thermal energy to the sample surface. In contrast, only a fraction of EUV photons are absorbed by a 40 nm thick film, and the absorption profile is comparatively uniform due to the weaker EUV-resist interaction relative to the electron-resist interaction. Consequently, the sample heating effect is much less pronounced in the case of EUV irradiation, effectively decoupling thermally-specific chemistry from photon-specific chemistry. Therefore, care must be taken in the interpretation of data resulting from electron-beam irradiation as a model for EUV-resist interactions, as thermal and photon-initiated reactions are inherently coupled.

Conclusions

In conclusion, we have rigorously evaluated the mechanisms underlying thermal and EUV-induced solubility switching of HfMAA nanoparticle photoresists based on a combination of IR spectroscopy, XPS, and DFT calculations. We find that PAB treatments commonly used to remove residual solvent from EUV resists lead to a loss of hydroxyl groups, formation of Hf-O bonds and bridging-chelating transformations in a fraction of the methacrylate ligands. The ultimate effect of these changes is to partially reduce the solubility of the films, an effect that is detrimental for patterning. Chemistry resulting from electron-beam irradiation, used as a model for understanding EUV-induced reactions, is more complicated, having both a thermal component and an electron-specific component. The electron-specific mechanism has been identified as a crosslinking process that is initiated when

methacrylate ligands coordinated to radical cations generated following EUV photon absorption decompose into CO_2 and propenyl radicals. The reaction between these propenyl radicals with unperturbed vinylic methylene result in the formation of larger radical structures that lead to crosslinks between adjacent clusters. IR spectra obtained via synchrotron-based IR microspectroscopy also show features associated with this crosslinking reaction, but do not show the spectral markers of thermally induced chemistry. This result highlights sample surface heating as an important aspect of electron-beam irradiation as a model for EUV chemistry that needs to be taken into account when studying photoresist mechanisms. These combined results have important implications for the development of HfMAA-based EUV photoresists and underline the importance of *in situ* probes for understanding EUV photoresist mechanisms and hybrid cluster reactions in general.

Supporting Information

Results on DFT calculations of HfMAA vibrational modes, solubility studies following different PAB conditions, IR spectra of benzoic acid substituted nanoclusters, details on the IR spectral analysis, and results from dynamic light scattering experiments can be found in the supporting information. This material is available free of charge via the internet at http://pubs.acs.org.

TOC Graphic

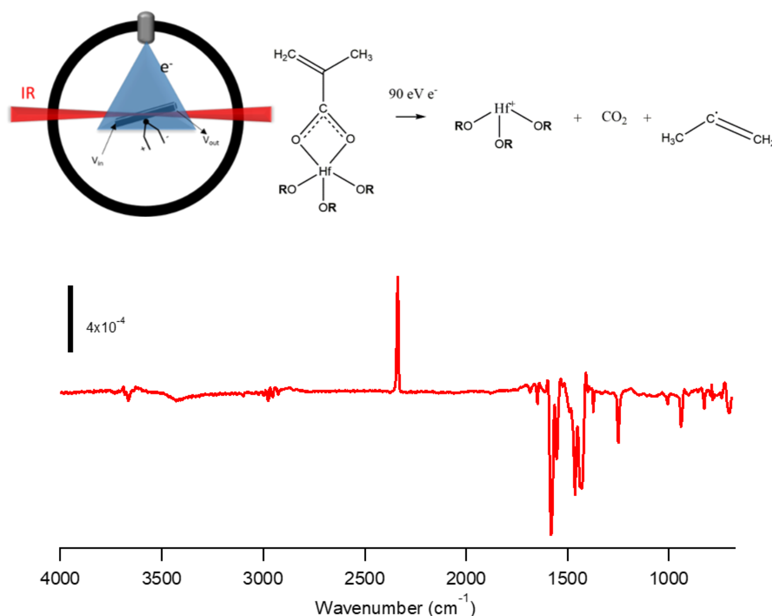

Figures

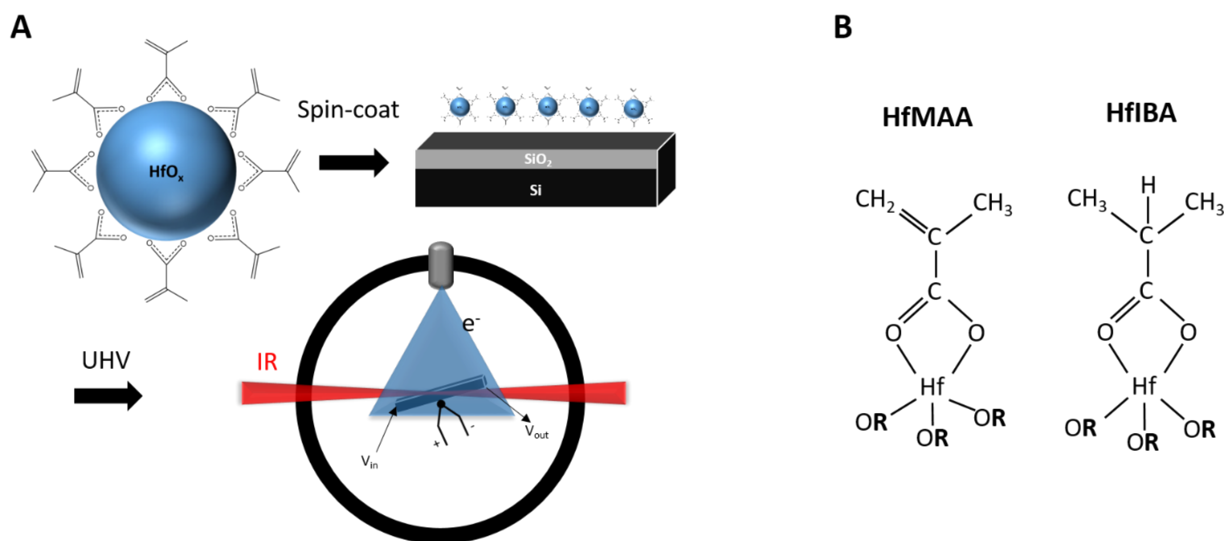

Figure 1: A) Schematic of HfMAA sample structure and *in situ* measurement scheme. B) Schematic representations of the chemical structure of HfMAA and HfIBA.

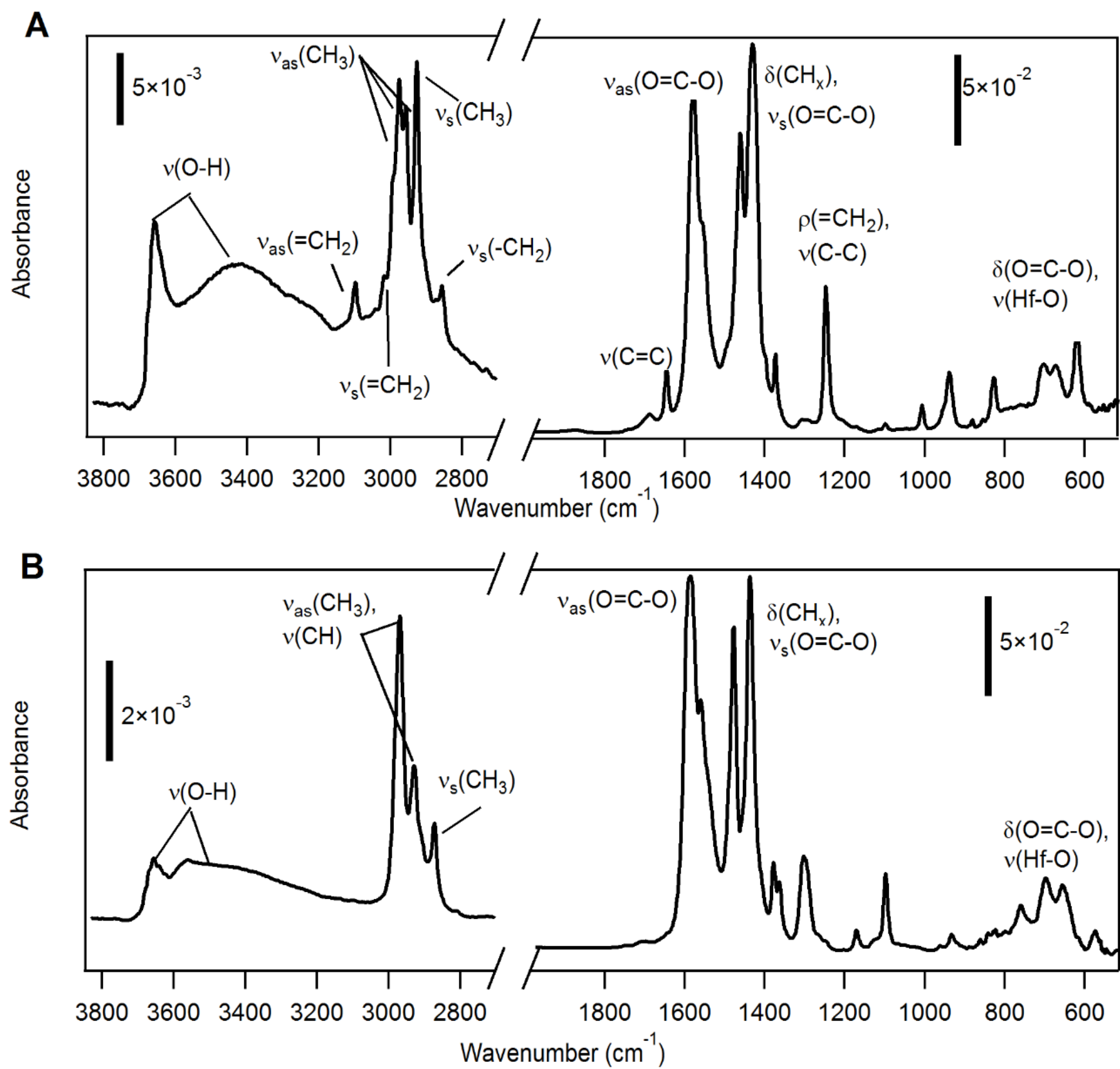

Figure 2: IR absorption spectra of as-prepared HfMAA (A) and HfIBA (B).

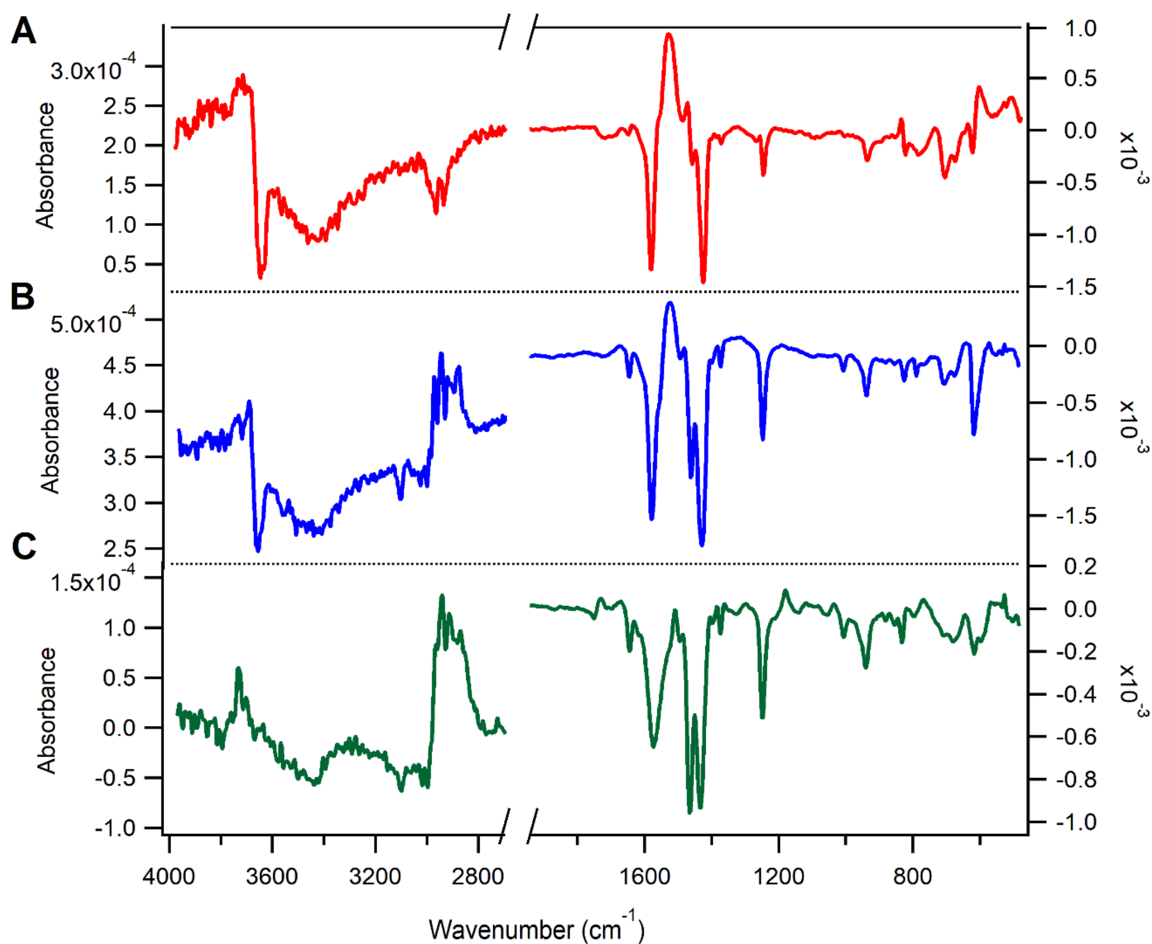

Figure 3: A) Differential absorption spectrum obtained following annealing of an HfMAA film to 105°C for 60 s under UHV referenced to the spectrum of the as-prepared material. B) Differential absorption spectrum obtained following irradiation of an HfMAA film with 40 $\mu C/cm^2$ of 90 eV electrons. Here, the sample investigated was first given a PAB using a hotplate programmed to 105°C under N_2 ambient for 60s prior to loading into the UHV chamber for electron irradiation. C) Differential absorption spectrum obtained following irradiation of an HfMAA film 40 $\mu C/cm^2$ of 90 eV electrons. In this case, the film was first subjected to a UHV PAB step, with a peak temperature of 105°C for 60 s, plus additional time to reach the target temperature.

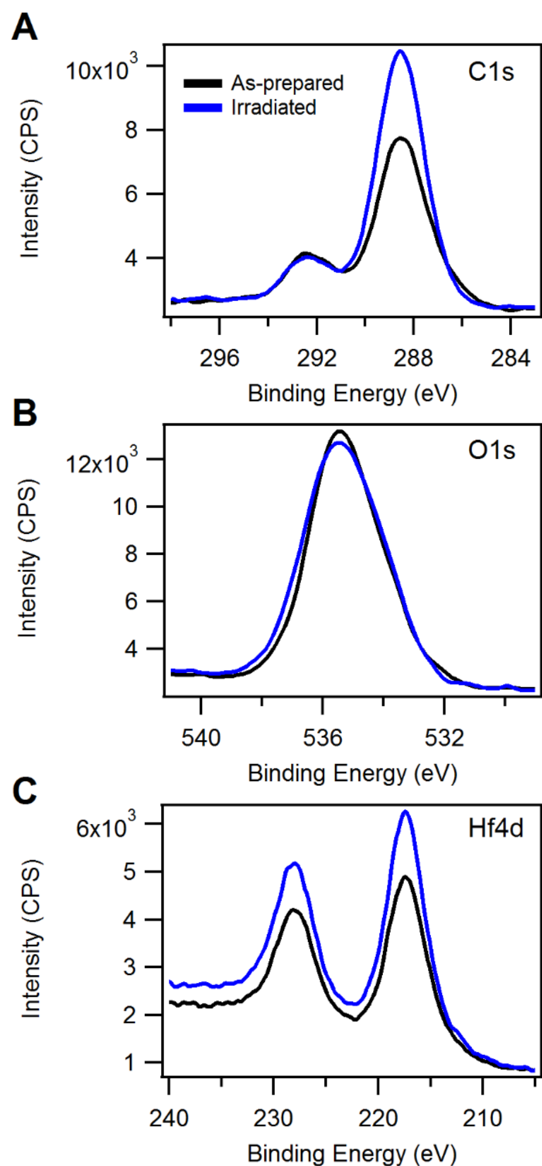

Figure 4: C1s (A), O1s (A) and Hf4d (C) photoemission spectra from HfMAA films as-prepared and following 90 eV irradiation.

	C1s	O1s	$Hf4d_{5/2}$
As-prepared	61.6±0.5	33.0±0.5	5.4±0.1
Irradiated	63.7±0.7	30.2±0.7	6.1±0.1

Table 1: Relative elemental composition calculated from the data in Fig. 4. The error bars were derived by taking the standard deviation of 3 measurements performed on different regions of the samples.

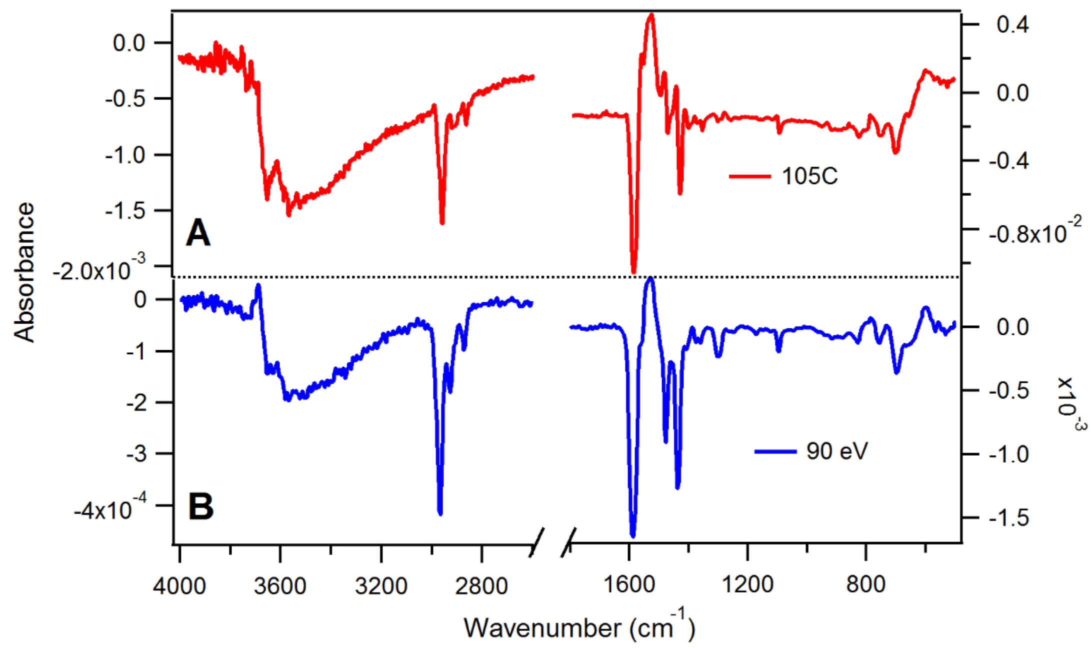

Figure 5: Differential absorption spectra of HfIBA films obtained upon A) 60 s resistive heating in UHV at 105°C, B) 90 eV electron beam irradiation with total dose of 41 μC/cm^2.

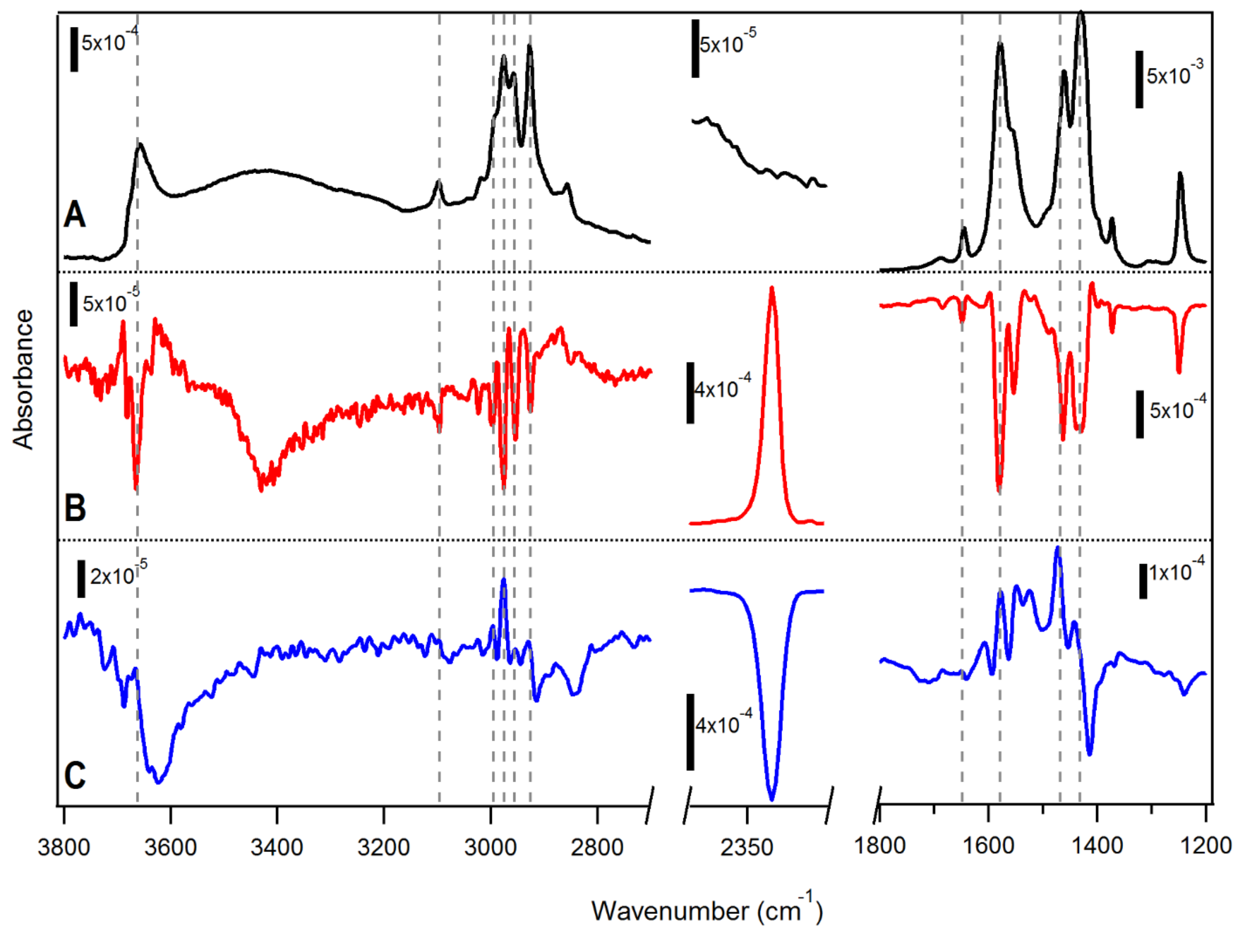

Figure 6: Low-temperature electron beam irradiation of HfMAA. A) *ex situ* IR spectrum of as-prepared HfMAA, for reference; B) differential spectrum obtained following 90 eV irradiation of HfMAA at 110K; C) differential spectrum obtained following annealing to 298K, referenced to the spectrum following irradiation (B).

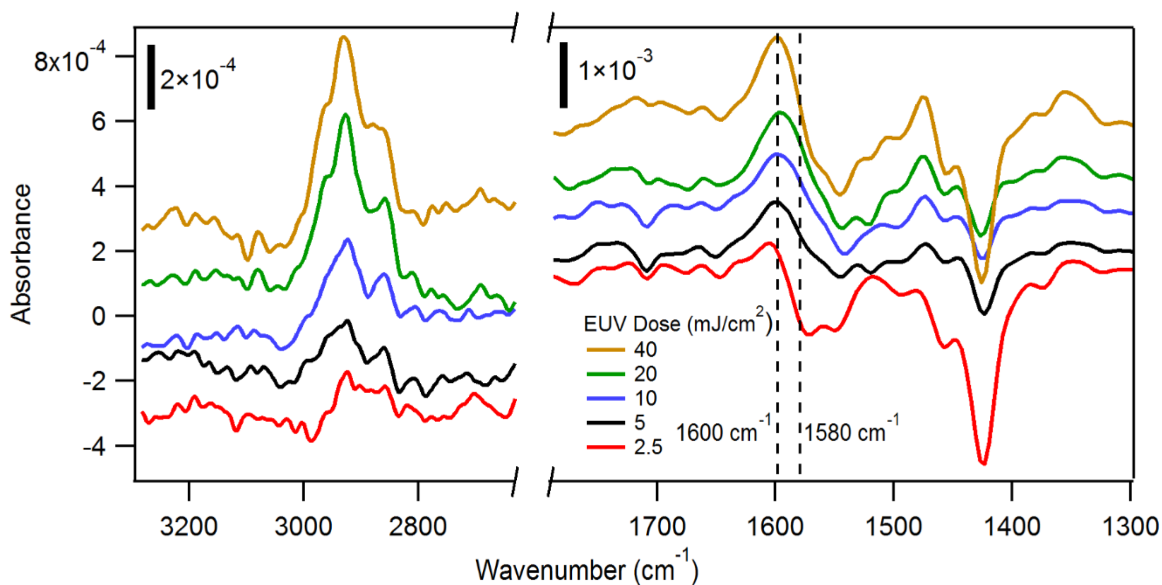

Figure 7: IR absorption difference between as-prepared HfMAA and HfMAA subjected to various EUV doses ranging from 2.5 – 40 mJ/cm^2. Here, the spectral subtraction is performed by scaling the spectra by the thickness of the films before irradiation so as to minimize any differences due to fluctuations of the starting film thickness. The data show in the carboxylate stretching region show a characteristic derivative lineshape, indicating a shift of the peak maximum from 1580 cm^{-1} to 1600 cm^{-1}.

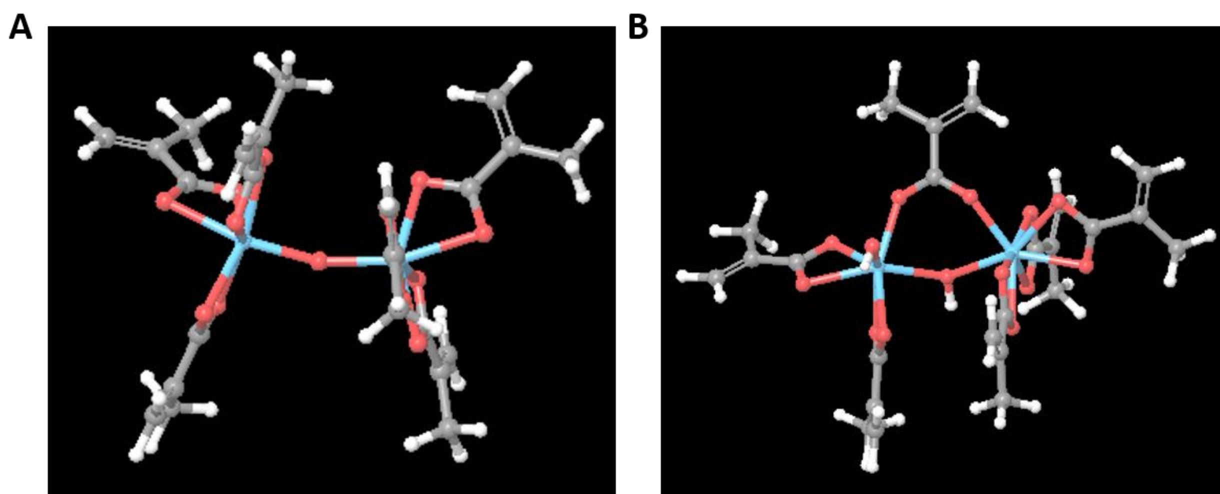

Figure 8: Cluster models used for understanding interaction between HfMAA and water vapor. A) represents the structure of the non-hydroxylated structure, while B) shows the structure following reaction with a water molecule to result in hydroxylation of the bridging O atom, incorporation of a terminal hydroxyl group, and conversion of one chelated ligand to a bridging ligand. Here, blue spheres represent Hf, red O, grey C and white H.

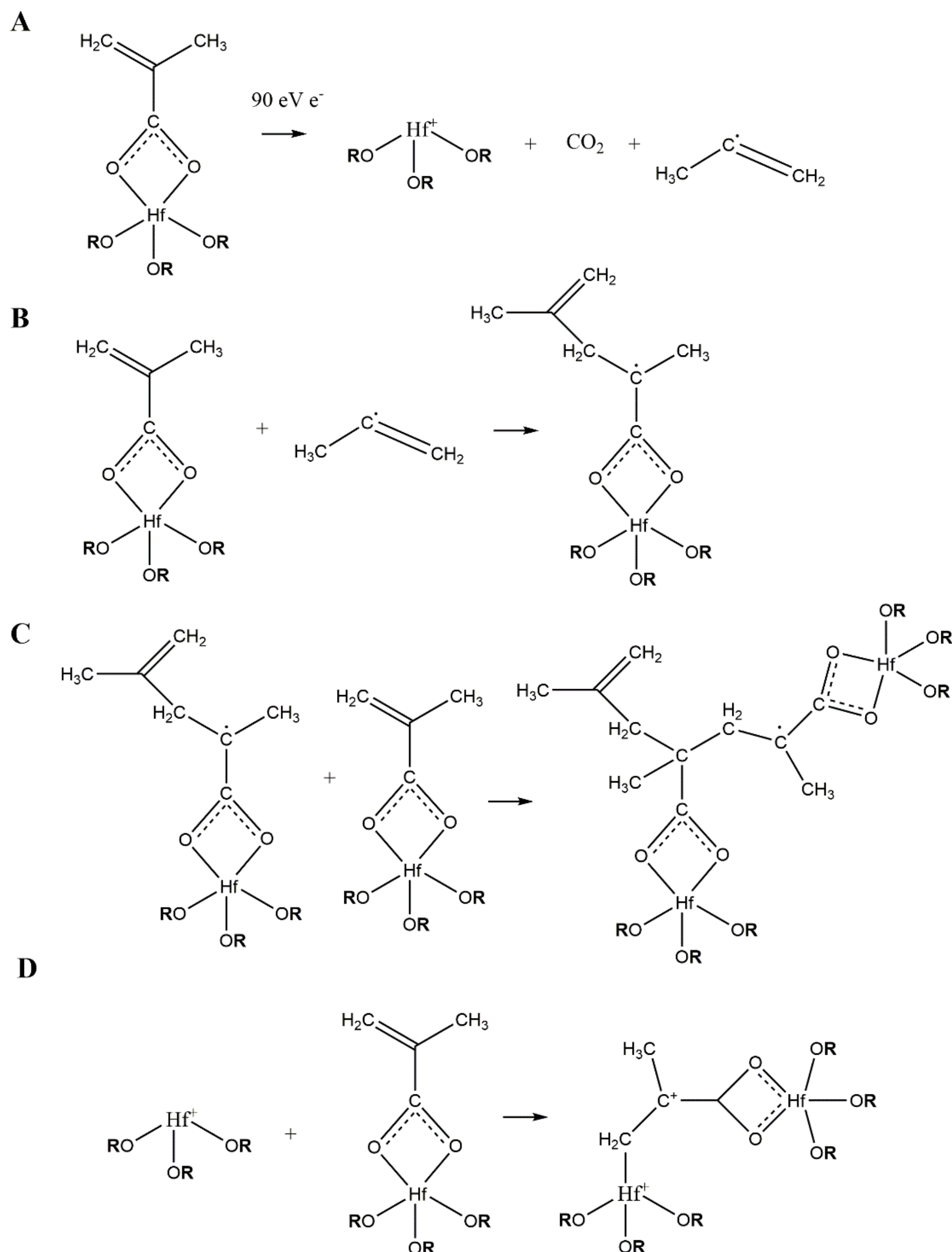

Figure 9: Proposed mechanism for solubility switching reactions induced by electron beam irradiation. A) Following interaction with energetic electrons (or similarly, EUV photon) ligand decomposition is initiated to produce a Hf cation, a CO_2 molecule, and a propenyl radical. B) Diffusion of the propenyl radical to a neighboring methacrylate ligand results in attachment via the vinylic methylene group, resulting in a larger radical ligand. C) The radical produced in B) can attach to a neighboring cluster via its vinylic group, thereby linking adjacent clusters and propagating the radical such that the cluster can participate in further reaction. D) In addition to the pathway described in B-C), crosslinking can also occur in a similar fashion via the cation that is generated in A). Here, the Hf cation reacts with the vinylic group of a neighboring cluster in a fashion analogous to the propenyl radical in B) to form a crosslinked cation structure that can participate in further reaction.

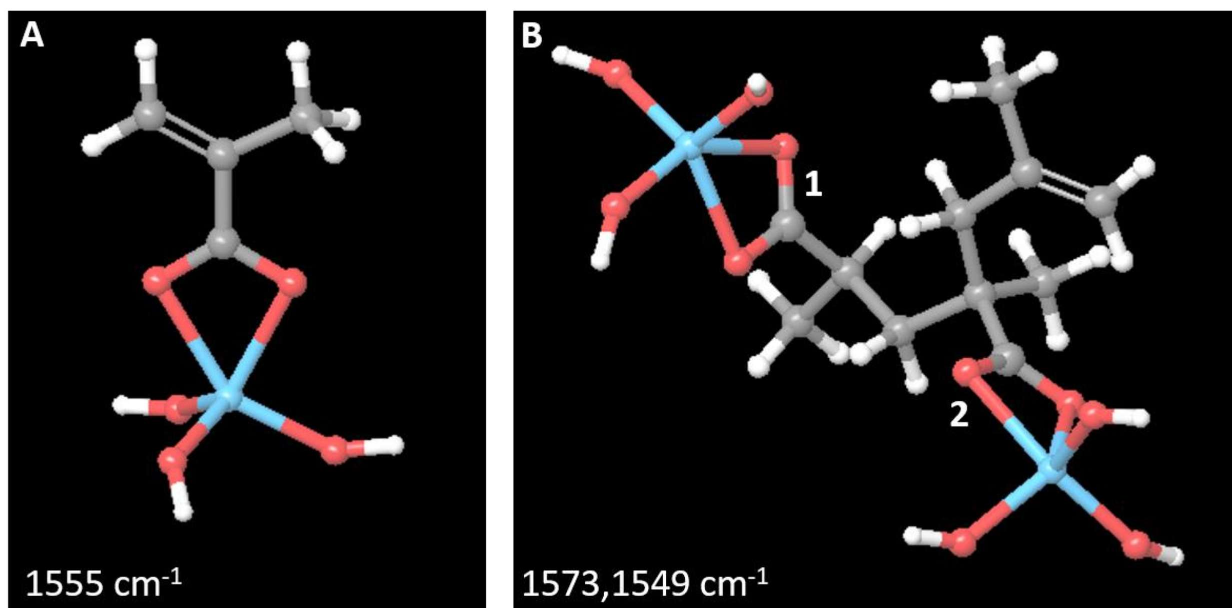

Figure 10: Cluster models and corresponding O-C=O stretching frequencies of DFT-optimized HfMAA clusters before (A) and after (B) a crosslinking reaction as depicted in Figs. 9A, B and D. The structure in (A) corresponds to the initial structure in Fig. 9A, and that in (B) corresponds to the final crosslinked structure in Fig. 9D.

Acknowledgements

This work was funded by the Semiconductor Research Corporation. This research used resources of the Advanced Light Source, which is a DOE Office of Science User Facility under contract no. DE-AC02-05CH11231.

References

1. Hoefflinger, B., ITRS: The International Technology Roadmap for Semiconductors. In *Chips 2020: A Guide to the Future of Nanoelectronics*, Hoefflinger, B., Ed. Springer Berlin Heidelberg: Berlin, Heidelberg, 2012; pp 161-174.
2. Bakshi, V., *EUV Lithography*. SPIE: Bellingham, WA, 2009.
3. Itani, T.; Kozawa, T., Resist Materials and Processes for Extreme Ultraviolet Lithography. *Jpn. J. Appl. Phys* **2013,** *52*.
4. Lio, A., EUV Resists: What's Next? In *Extreme Ultraviolet*, Panning, E. M.; Goldberg, K. A., Eds. Spie-Int Soc Optical Engineering: Bellingham, 2016; Vol. 9776.
5. Fujii, S.; Okamoto, K.; Yamamoto, H.; Kozawa, T.; Itani, T., Sensitivity enhancement of chemically amplified EUV resists by adding acid-generating promoters. *Jpn. J. Appl. Phys* **2017,** *56*.
6. Li, L.; Liu, X.; Pal, S.; Wang, S. L.; Ober, C. K.; Giannelis, E. P., Extreme ultraviolet resist materials for sub-7 nm patterning. *Chem. Soc. Rev.* **2017,** *46*, 4855-4866.
7. Kozawa, T.; Saeki, A.; Tagawa, S., Point spread function for the calculation of acid distribution in chemically amplified resists for extreme ultraviolet lithography. *Appl. Phys. Express* **2008,** *1*.
8. Jiang, J.; De Simone, D.; Yildirim, O.; Meeuwissen, M.; Hoefnagels, R.; Rispens, G.; Custers, R.; Derks, P., Impact of acid statistics on EUV local critical dimension uniformity. In *Extreme Ultraviolet*, Panning, E. M.; Goldberg, K. A., Eds. Spie-Int Soc Optical Engineering: Bellingham, 2017; Vol. 10143.
9. Krysak, M.; Trikeriotis, M.; Schwartz, E.; Lafferty, N.; Xie, P.; Smith, B.; Zimmerman, P.; Montgomery, W.; Giannelis, E.; Ober, C. K., Development of an Inorganic Nanoparticle Photoresist for EUV, E-beam and 193 nm Lithography. In *Advances in Resist Materials and Processing Technology Xxviii*, Allen, R. D.; Somervell, M. H., Eds. Spie-Int Soc Optical Engineering: Bellingham, 2011; Vol. 7972.
10. Goberna-Ferron, S.; Park, D. H.; Amador, J. M.; Keszler, D. A.; Nyman, M., Amphoteric Aqueous Hafnium Cluster Chemistry. *Angew. Chem. Int. Ed.* **2016,** *55*, 6221-6224.
11. Kasahara, K.; Xu, H.; Kosma, V.; Odent, J.; Giannelis, E. P.; Ober, C. K., Nanoparticle photoresist studies for EUV lithography. In *Extreme Ultraviolet*, Panning, E. M.; Goldberg, K. A., Eds. Spie-Int Soc Optical Engineering: Bellingham, 2017; Vol. 10143.
12. Trikeriotis, M.; Krysak, M.; Chung, Y. S.; Ouyang, C.; Cardineau, B.; Brainard, R.; Ober, C. K.; Giannelis, E. P.; Cho, K. A new inorganic EUV resist with high-etch resistance, In *SPIE Advanced Lithography*, Proc. SPIE, 2012; 8322, 83220U.
13. De Simone, D.; Sayan, S.; Dei, S.; Pollentier, I.; Kuwahara, Y.; Vandenberghe, G.; Nafus, K.; Shiratani, M.; Nakagawa, H.; Naruoka, T., Novel metal containing resists for EUV lithography extendibility. In *Extreme Ultraviolet*, Panning, E. M.; Goldberg, K. A., Eds. Spie-Int Soc Optical Engineering: Bellingham, 2016; Vol. 9776.
14. Kasahara, K.; Xu, H.; Kosma, V.; Odent, J.; Giannelis, E. P.; Ober, C. K., Recent Progress in EUV Metal Oxide Photoresists. *J. Photopolym. Sci. Technol.* **2017,** *30*, 93-97.
15. Oleksak, R. P.; Ruther, R. E.; Luo, F. X.; Fairley, K. C.; Decker, S. R.; Stickle, W. F.; Johnson, D. W.; Garfunkel, E. L.; Herman, G. S.; Keszler, D. A., Chemical and Structural Investigation of High-Resolution Patterning with HafSOx. *ACS Appl. Mater. Interfaces* **2014,** *6*, 2917-2921.
16. Fallica, R.; Stowers, J. K.; Grenville, A.; Frommhold, A.; Robinson, A. P. G.; Ekinci, Y. Dynamic absorption coefficients of CAR and non-CAR resists at EUV, In *SPIE Advanced Lithography*, Proc. SPIE, 2016; 9776, 977612.
17. Trikeriotis, M.; Krysak, M.; Chung, Y. S.; Ouyang, C.; Cardineau, B.; Brainard, R.; Ober, C. K.; Giannelis, E. P.; Cho, K., Nanoparticle Photoresists from HfO_2 and ZrO_2 for EUV Patterning. *J. Photopolym. Sci. Technol.* **2012,** *25*, 583-586.

18. Wood, O. R.; Panning, E. M.; Ober, C.; Jiang, J.; Zhang, B.; Li, L.; Giannelis, E.; Chun, J. S.; Neisser, M.; Sierra-Alvares, R. New developments in ligand-stabilized metal oxide nanoparticle photoresists for EUV lithography, In *SPIE Advanced Lithography*, Proc. SPIE, 2015; 9422, 942207.
19. Li, L.; Chakrabarty, S.; Spyrou, K.; Ober, C. K.; Giannelis, E. P., Studying the Mechanism of Hybrid Nanoparticle Photoresists: Effect of Particle Size on Photopatterning. *Chem. Mater.* **2015,** *27*, 5027-50310.
20. Li, L.; Chakrabarty, S.; Jiang, J.; Zhang, B.; Ober, C.; Giannelis, E. P., Solubility studies of inorganic-organic hybrid nanoparticle photoresists with different surface functional groups. *Nanoscale* **2016,** *8*, 1338-1343.
21. Krysak, M.; Trikeriotis, M.; Ouyang, C.; Chakrabarty, S.; Giannelis, E. P.; Ober, C. K., Nanoparticle Photoresists: Ligand Exchange as a New, Sensitive EUV Patterning Mechanism. *J. Photopolym. Sci. Technol.* **2013,** *26*, 659-664.
22. Ober, C. K.; Xu, H.; Kosma, V.; Sakai, K.; Giannelis, E. P. EUV photolithography: resist progress and challenges, In *SPIE Advanced Lithography*, Proc. SPIE, 2018; 10583, 1058306.
23. Chakrabarty, S.; Ouyang, C.; Krysak, M.; Trikeriotis, M.; Cho, K.; Giannelis, E. P.; Ober, C. K. Oxide nanoparticle EUV resists: toward understanding the mechanism of positive and negative tone patterning, In *SPIE Advanced Lithography*, Proc. SPIE, 2013; 8679, 867906.
24. Kosma, V.; Kasahara, K.; Xu, H.; Sakai, K.; Ober, C.; Giannelis, E. Patterning mechanism of metal based hybrid EUV resists, In *SPIE Advanced Lithography*, Proc. SPIE, 2018; 10583, 105831U.
25. Castellanos, S.; Wu, L.; Baljozovic, M.; Portale, G.; Kazazis, D.; Vockenhuber, M.; Ekinci, Y.; Jung, T. Ti, Zr, and Hf-based molecular hybrid materials as EUV photoresists, In *SPIE Advanced Lithography*, Proc. SPIE, 2018; 10583, 105830A.
26. Grzeskowiak, S.; Narasimhan, A.; Murphy, M.; Ackerman, C.; Kaminsky, J.; Brainard, R. L.; Denbeaux, G., Analytical Techniques for Mechanistic Characterization of EUV Photoresists. In *Advances in Patterning Materials and Processes Xxxiv*, Hohle, C. K., Ed. Spie-Int Soc Optical Engineering: Bellingham, 2017; Vol. 10146.
27. Grzeskowiak, S.; Narasimhan, A.; Rebeyev, E.; Joshi, S.; Brainard, R. L.; Denbeaux, G., Acid Generation Efficiency of EUV PAGs via Low Energy Electron Exposure. *J. Photopolym. Sci. Technol.* **2016,** *29*, 453-458.
28. Murphy, M.; Narasimhan, A.; Grzeskowiak, S.; Sitterly, J.; Schuler, P.; Richards, J.; Denbeaux, G.; Brainard, R. L., EUV Mechanistic Studies of Antimony Resists. *J. Photopolym. Sci. Technol.* **2017,** *30*, 121-131.
29. Torok, J.; Srivats, B.; Memon, S.; Herbol, H.; Schad, J.; Das, S.; Ocola, L.; Denbeaux, G.; Brainard, R. L., Electron Penetration Depths in EUV Photoresists. *J. Photopolym. Sci. Technol.* **2014,** *27*, 611-615.
30. *Materials Science Suite Version 2017-2*, Schrodinger, LLC: New York, NY, 2017.
31. *Jaguar, Version 9.8*, Schrodinger, LLC: New York, NY, 2017.
32. Bochevarov, A. D.; Harder, E.; Hughes, T. F.; Greenwood, J. R.; Braden, D. A.; Philipp, D. M.; Rinaldo, D.; Halls, M. D.; Zhang, J.; Friesner, R. A., Jaguar: A high-performance quantum chemistry software program with strengths in life and materials sciences. *Int. J. Quantum Chem* **2013,** *113*, 2110-2142.
33. Lee, C. T.; Yang, W. T.; Parr, R. G., Development of the Colle-Salvetti correlation-energy formula into a functional of the electron density. *Phys. Rev. B* **1988,** *37*, 785-789.
34. Hay, P. J.; Wadt, W. R., *Ab initio* effective core potentials for molcular calculations. Potentials for K to Au including outermost core orbitals. *J. Chem. Phys.* **1985,** *82*, 299-310.
35. Becke, A. D., Density-functional thermochemistry. III. The role of exact exchange. *J. Chem. Phys.* **1993,** *98*, 5648-5652.

36. Park, H. H.; Choi, D. G.; Zhang, X.; Jeon, S.; Park, S. J.; Lee, S. W.; Kim, S.; Kim, K. D.; Choi, J. H.; Lee, J.; Yun, D. K.; Lee, K. J.; Park, H. H.; Hill, R. H.; Jeong, J. H., Photo-induced hybrid nanopatterning of titanium dioxide via direct imprint lithography. *J. Mater. Chem.* **2010,** *20*, 1921-1926.
37. Stehlin, F.; Wieder, F.; Spangenberg, A.; Le Meins, J. M.; Soppera, O., Room-temperature preparation of metal-oxide nanostructures by DUV lithography from metal-oxo clusters. *J. Mater. Chem. C.* **2014,** *2*, 277-285.
38. Kickelbick, G.; Schubert, U., Inorganic clusters in organic polymers and the use of polyfunctional inorganic compounds as polymerization initiators. *Monatsh. Chem.* **2001,** *132*, 13-30.
39. Schubert, U.; Volkel, T.; Moszner, N., Mechanical properties of an inorganic-organic hybrid polymer cross-linked by the cluster $Zr_4O_2(methacrylate)_{12}$. *Chem. Mater.* **2001,** *13*, 3811-3812.
40. Trimmel, G.; Gross, S.; Kickelbick, G.; Schubert, U., Swelling behavior and thermal stability of poly(methylmethacrylate) crosslinked by the oxozirconium cluster $Zr_4O_2(methacrylate)_{12}$. *Appl. Organomet. Chem.* **2001,** *15*, 401-406.
41. Gross, S.; Kickelbick, G.; Puchberger, M.; Schubert, U., Mono-, Di-, and Trimetallic Methacrylate-substituted Metal Oxide Clusters Derived from Hafnium Butoxide. *Monatsh. Chem.* **2003,** *134*, 1053-1063.